

Structural basis of Mcm2–7 replicative helicase loading by ORC–Cdc6 and Cdt1

Zuanning Yuan^{1,7}, Alberto Riera^{2,3,7}, Lin Bai^{1,7}, Jingchuan Sun¹, Saikat Nandi⁴, Christos Spanos⁵, Zhuo Angel Chen⁵, Marta Barbon^{2,3}, Juri Rappsilber^{5,6}, Bruce Stillman⁴, Christian Speck^{2,3} & Huilin Li¹

To initiate DNA replication, the origin recognition complex (ORC) and Cdc6 load an Mcm2–7 double hexamer onto DNA. Without ATP hydrolysis, ORC–Cdc6 recruits one Cdt1-bound Mcm2–7 hexamer, thus forming an ORC–Cdc6–Cdt1–Mcm2–7 (OCCM) helicase-loading intermediate. Here we report a 3.9-Å structure of *Saccharomyces cerevisiae* OCCM on DNA. Flexible Mcm2–7 winged-helix domains (WHDs) engage ORC–Cdc6. A three-domain Cdt1 configuration embraces Mcm2, Mcm4, and Mcm6, thus comprising nearly half of the hexamer. The Cdt1 C-terminal domain extends to the Mcm6 WHD, which binds the Orc4 WHD. DNA passes through the ORC–Cdc6 and Mcm2–7 rings. Origin DNA interaction is mediated by an α -helix within Orc4 and positively charged loops within Orc2 and Cdc6. The Mcm2–7 C-tier AAA+ ring is topologically closed by an Mcm5 loop that embraces Mcm2, but the N-tier-ring Mcm2–Mcm5 interface remains open. This structure suggests a loading mechanism of the first Cdt1-bound Mcm2–7 hexamer by ORC–Cdc6.

The *S. cerevisiae* ORC is an ATPase complex composed of Orc1–6 (refs. 1–3). The composition and architecture of ORC are conserved in all eukaryotes⁴. Low-resolution electron microscopy (EM) images showed that the six subunits are arranged into a crescent shape in the order Orc1, Orc4, Orc5, Orc3, Orc2, with Orc6 binding to Orc2/Orc3 (refs. 5,6). This architecture was confirmed by a recent crystal structure of an inactive *Drosophila* ORC (DmORC)⁷. The DmORC core is a notched two-tiered ring composed of an N-tier ring of five AAA+ domains and a C-tier ring of five WHDs of Orc1–5. Because the DmORC1 AAA+ domain blocks the putative central DNA-binding channel in the autoinhibited conformation⁷, the configuration of an active ORC could not be determined. Replication origins are bound by the budding yeast ORC throughout the cell-division cycle¹, but they are ‘licensed’ during the G1 phase⁸. An early step is the binding of initiation factor Cdc6 to DNA-bound ORC to form the ORC–Cdc6–DNA complex⁹. EM studies have shown that Cdc6 closes a gap in the crescent-shaped ORC to form a ring^{9,10} and apparently activates a molecular switch in ORC, converting it from an origin-DNA binder to an active Mcm2–7 loader^{6,9}. However, the physical nature of the molecular switch is currently unknown owing to the lack of a high-resolution structure of ORC–Cdc6 on DNA.

The next steps involve the sequential recruitment of two Cdt1-bound hexamers of Mcm2–7 onto the origin DNA by ORC–Cdc6 to form an Mcm2–7 double hexamer (DH) that composes part of the pre-replication complex (pre-RC)^{8,11}. *In vitro* reactions with purified components have demonstrated that a high salt-stable Mcm2–7 DH

is loaded on DNA in an ATP-dependent manner^{12,13}. All hexamers within the DH are assembled in such a way that their respective Mcm3 and Mcm6 subunits face each other, as revealed by EM images of maltose-binding protein (MBP)-tagged DH as well as a 3.8-Å resolution cryo-EM structure^{14,15}. The Mcm2–7 DH has a central channel that is wide enough to allow the passage of double-stranded DNA (dsDNA), in agreement with biochemical findings^{12,13}. Because the two Mcm2–7 hexamers are twisted with respect to each other, it was speculated that within the interface between the two hexamers, an inflection point of the DNA path is created, possibly promoting melting of the dsDNA when the helicase becomes activated in S phase¹⁴. At the G1-to-S transition, the inactive DH is converted into an active replicative helicase that consists of an Mcm2–7 hexamer bound to Cdc45 and the four-subunit GINS complex, called the CMG^{16,17}. Disruption of the Mcm2–7 DH and assembly of the CMG require activation by the Dbf4–Cdc7 protein kinase and cyclin-dependent kinase (Clb5–Cdc28), which phosphorylate some of the pre-RC components, including Mcm2–7 subunits and the accessory loading proteins Sld2 and Sld3 (refs. 1,8,18–26). Subsequently, primase and DNA polymerases load, along with many other replication factors, to form the replisome that executes DNA synthesis^{27,28}.

The two Mcm2–7 hexamers are loaded on DNA sequentially^{15,29,30}. In the presence of ATP γ S, ORC–Cdc6 loads the first Mcm2–7 hexamer on DNA, thus forming the OCCM intermediate^{15,31}. Then ATP hydrolysis is triggered, and Cdc6 and Cdt1 are released^{30,32–34}. Single-molecule analysis suggests that a second Cdc6 protein is

¹Cryo-EM Structural Biology Laboratory, Van Andel Research Institute, Grand Rapids, Michigan, USA. ²MRC London Institute of Medical Sciences (LMS), London, UK. ³DNA Replication Group, Institute of Clinical Sciences (ICS), Faculty of Medicine, Imperial College London, London, UK. ⁴Cold Spring Harbor Laboratory, Cold Spring Harbor, New York, USA. ⁵Wellcome Trust Centre for Cell Biology, University of Edinburgh, Edinburgh, UK. ⁶Chair of Bioanalytics, Institute of Biotechnology, Technische Universität Berlin, Berlin, Germany. ⁷These authors contributed equally to this work. Correspondence should be addressed to J.R. (juri.rappsilber@ed.ac.uk), B.S. (stillman@cshl.edu), C. Speck (chris.speck@imperial.ac.uk) or H.L. (Huilin.Li@vai.org).

Received 2 December 2016; accepted 9 January 2017; published online 13 February 2017; doi:10.1038/nsmb.3372

recruited to the ORC, which functions to load a second Cdt1-bound Mcm2–7 to form an ORC–Cdc6–Mcm2–7–Mcm2–7 complex before Mcm2–7 DH formation^{15,30,35}. *In vivo* evidence suggests that ATP hydrolysis by Cdc6 causes the separation of the DH from ORC–Cdc6 (ref. 36). In this work, we describe a 3.9-Å-resolution cryo-EM structure of the 1.1-MDa 14-protein OCCM complex on DNA, as well as mass-spectrometry-based observations of interactions between individual proteins. The structure reveals how ORC–Cdc6 recognizes origin DNA and how this complex recruits the first Cdt1-bound Mcm2–7 hexamer, thereby illuminating a crucial step in eukaryotic DNA-replication initiation.

RESULTS

Overall structure of the OCCM–DNA complex

We prepared the OCCM complexes in the presence of ATP γ S from purified proteins on a replication-origin-containing plasmid attached to magnetic beads. After DNase I treatment, the OCCM samples were released from the beads and directly processed for cryo-EM grid preparation. We derived a 3.9-Å-resolution cryo-EM 3D map of the OCCM from 304,288 particles that were selected from 7,500 raw electron micrographs, and nearly 1,000,000 raw particles that were recorded on a K2 camera in a Titan Krios microscope operated at a high tension of 300 kV (Fig. 1a–c, Supplementary Figs. 1–3, Table 1, Supplementary Video 1, and Online Methods). The 3D map had well-defined densities for the dsDNA and 13 subunits of the 14-protein complex (Fig. 1d,e). The only protein that was not well resolved was Orc6; its density was visible only at a lower display threshold. Nevertheless, a conserved C-terminal α -helix of Orc6 was resolved, which is important, as it is mutated in Meier–Gorlin syndrome^{37,38}. To better understand the architecture of the complex, and particularly of the flexible sections involving Orc6, we carried out cross-linking/mass spectrometry (CLMS) analysis, which confirmed the general architecture and also identified several interactions between Orc6 and Orc2/Mcm2 (Fig. 2a–c, Supplementary Fig. 4, and Supplementary Data Sets 1 and 2). We built an atomic model of the OCCM into the EM densities, with guidance from the published structures of the Mcm2–7 hexamer¹⁴, the DmORC⁷, an archaeal Cdc6 homolog³⁹, a homolog of the N-terminal domain (NTD) of Cdt1, and the middle helical domain (MHD) and C-terminal domain (CTD) of human Cdt1 (refs. 40–42). The dsDNA was manually built into the EM density (Supplementary Fig. 5). Electron densities for eight nucleotides were observed at the Mcm2–Mcm6, Mcm6–Mcm4, Mcm4–Mcm7, Mcm7–Mcm3, Cdc6–Orc1, Orc1–Orc4, Orc4–Orc5, and Orc5–Orc3 interfaces (Supplementary Fig. 6). No nucleotide densities were resolved at interfaces between Mcm3 and Mcm5 or between Mcm5 and Mcm2 because of the reduced resolution and increased flexibility, as they were either at or near the DNA-loading gate.

In the top ORC–Cdc6 tier of the OCCM, Orc1–5 and Cdc6 formed a six-membered ring structure, with Cdc6 bridging the gap between Orc1 and Orc2, in agreement with a previous, lower-resolution EM study⁵ (Fig. 3). Interestingly, four WHDs of Mcm3, Mcm4, Mcm6, and Mcm7 spiraled upward from the Mcm2–7 hexamer and engaged the ORC–Cdc6 ring, each interacting with ORC–Cdc6 subunits (Fig. 1d,e and Supplementary Fig. 7), and we observed an interaction between the Mcm5 WHD and Orc2 via CLMS (Fig. 2c). In the bottom Cdt1–Mcm2–7 tier, the six Mcm subunits formed a ring structure (order: Mcm2, Mcm6, Mcm4, Mcm7, Mcm3, Mcm5), in agreement with previous studies^{14,15,22,43,44}. At the interface between the Mcm2 AAA+ domain and the Mcm5 AAA+ domain, the domain-swapped α -helix of Mcm5 bound to the Mcm2 AAA+ domain, thereby topologically closing the DNA-loading gate (Fig. 1c,d and Supplementary Fig. 8).

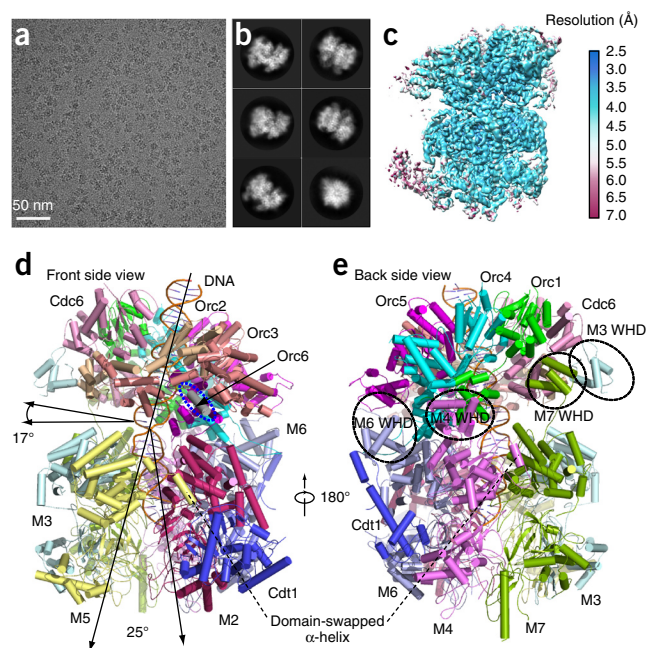


Figure 1 Cryo-EM images and overall structure of the *S. cerevisiae* OCCM complex. (a) A representative motion-corrected raw image of frozen OCCM particles recorded on a direct detector. (b) Six selected 2D averages representing the particles in different views. (c) A 3D cryo-EM map of OCCM, color-coded to show local resolution. The overall resolution is 3.9 Å. (d) Cartoon view of the atomic model of OCCM as viewed from the front side. The two arrows pointing to the left indicate that the ORC–Cdc6 ring lies on the Mcm ring, tilted by an angle of ~17°. The two black arrows in the middle show that the DNA in the central channel is bent by ~25°. The blue dashed oval marks the short helix of Orc6. (e) Cartoon view of the OCCM model as viewed from the back side. The black ovals mark the WHDs of Mcm3, Mcm4, Mcm6, and Mcm7. In d and e, “M” stands for “Mcm.”

However, the N-tier ring was still open at the Mcm2–5 interface. Hence Mcm2–7 was in a half-open, half-closed state. This structural feature explains why the Mcm2–7 ring in the OCCM is partially salt stable on DNA, but not as salt stable as the Mcm2–7 DH^{15,31,44}. The structure also explains why the DNA is intact in the C-tier AAA+ ring but invisible in the N-tier ring, as DNA in this region may be less constrained or be digested by the nuclease used to release the DNA-bound OCCM during sample preparation.

ORC–Cdc6 forms a closed ring with a pseudo-six-fold symmetry

In the OCCM structure, ORC–Cdc6 assembled into a complete ring encircling DNA with a pseudo-six-fold symmetry (Figs. 3a,b and 4). The N-terminal extension on Orc2 and an insertion in Orc3 give the ORC a helical shape⁴⁴. The four observed ATP γ S molecules of ORC–Cdc6 define one circle on top, and the four observed nucleotides in Mcm2–7 define another circle below. The top circle is larger, off center, and tilted by 17° with respect to the lower circle (Fig. 4a,b). The six predicted AAA+ proteins, Orc1–5 and Cdc6, all had one AAA+ domain with an AAA–RecA fold (the RecA fold), an α -helical-lid domain (the lid), and a C-terminal α -helical WHD, and they were superimposable^{45,46} (Fig. 3c). There were variations on this general rule; for example, Orc2 lacked the α -helical lid, similar to DmOrc2, and Orc3 had an insertion consisting of a helical domain. Among the six initiator AAA+ subunits, Orc4 was unique in that it had one α -helix insertion and one insertion loop in the WHD. The six AAA–RecA folds and the six WHDs formed a two-tiered ring

Table 1 Cryo-EM data collection and refinement statistics

<i>S. cerevisiae</i> OCCM complex (EMD-8540, PDB 5UDB)	
Data collection	
EM equipment	FEI Titan Krios
Voltage (kV)	300
Detector	Gatan K2
Pixel size (Å)	1.01
Electron dose (e ⁻ /Å ²)	50
Defocus range (μm)	1.5–3.5
Reconstruction	
Software	RELION 1.4
Number of particles used	304,288
Resolution (Å)	3.9
Map-sharpening <i>B</i> factor (Å ²)	123
Model composition	
Peptide chains	14
Protein residues	6,869
Nucleotides	78
R.m.s. deviation	
Bond length (Å)	0.007
Bond angle (°)	1.292
Ramachandran plot	
Preferred (%)	89.45
Allowed (%)	9.09
Outlier (%)	1.46
Validation	
MolProbity score	2.59 (97%)
Good rotamer (%)	95.65%
Clashscore, all atoms	34.88 (75%)

structure that surrounded the DNA within the central channel. In contrast, the six AAA-lid domains that each bridged the AAA-RecA-like domain and the WHD formed an outer brace that spiraled around the DNA-interacting domains. The bottom-tier ring of the WHDs was largely responsible for interacting with the Mcm CTDs below, as suggested in a previous study⁷. The peripheral brace of the AAA lids also interacted with the Mcm subunit WHDs.

The crystal structure of the DmORC core revealed a conformation that is not compatible with DNA binding⁷ (Fig. 3d). The DmORC structure is also incompatible with Cdc6 binding. However, we found that Orc3–5 were in a similar configuration in both *S. cerevisiae* ORC and DmORC. By aligning the two ORC structures, using the common Orc3–5 region as a reference, we found that the RecA fold of DmOrc1 and the WHD of DmOrc2 needed to move and flip by ~180° in order to match their respective yeast counterparts (Fig. 3e,f). These changes created a gap between Orc1 and Orc2 for DNA passage as well as for Cdc6 insertion between Orc1 and Orc2 after DNA binding by ORC (Fig. 3b,d and Supplementary Video 2). Because the Mcm2–7 hexamer had been loaded onto DNA by ORC–Cdc6, the conformation of ORC–Cdc6 in the OCCM structure is clearly in its active form, thus allowing DNA binding⁹ and both Cdc6–Orc1 and Orc1–Orc4 ATPase activities that are required for Mcm2–7 DH assembly or subsequent regulated initiation of DNA replication once per cell-division cycle^{9,29,30,32,47,48}.

Cdt1 forms an extended three-domain structure

In the OCCM structure, Cdt1 exists in an unusually extended three-domain structure (Fig. 5a–c). The density of the Cdt1 NTD was relatively weak, which indicated a degree of flexibility. The Cdt1 NTD bound only to the Mcm2 CTD with an interface of ~600 Å².

Surprisingly, the Cdt1 CTD was linked to the MHD by a long loop and was 60 Å away from the MHD, located between Mcm6 and Mcm4. In contrast, the Cdt1 MHD bound to both the NTD and the CTD of Mcm2 as well as to the NTD of Mcm6 with a larger interface of ~1,000 Å², which was also noted in the CLMS experiment (Fig. 2a). The Cdt1 CTD interacted extensively with all of the major domains of Mcm6, the Mcm4 NTD, and the Orc4 WHD insertion loop. Consistent with this observation, a previous NMR spectroscopy study showed interaction between the Mcm6 WHD and a short peptide in the CTD of Cdt1 (ref. 40). Importantly, the Cdt1 CTD formed an arch extending toward the Mcm6 WHD, which in turn interacted with the Orc4 WHD and the Orc5 AAA lid. The Mcm6 WHD in the Mcm2–7 hexamer before encountering ORC–Cdc6 is likely to be located in the middle of the ring between Mcm2 and Mcm6, because this is where the domain is found both in the active helicase CMG and in the inactive Mcm2–7 DH (Fig. 5d). Hence, the C-terminal arch of Cdt1 is probably responsible for displacing the Mcm6 WHD by 40 Å to the periphery, where the Mcm6 WHD is found in the OCCM structure. It is likely that this conformational change explains the inhibitory role of the Mcm6 WHD, which blocks OCCM formation in the absence of Cdt1 (ref. 32). Therefore, Cdt1 seems to have had a dual role in Mcm2–7 hexamer loading: it created the ORC–Cdc6-binding surface on the C-terminal surface of the Mcm2–7 hexamer by moving the obstructing Mcm6 WHD outward, and at the same time it formed an extended three-domain side brace that stabilized the Mcm2–Mcm6–Mcm4 half-ring, thereby potentially allowing the other half-ring (Mcm5–Mcm3–Mcm7) to move (Fig. 1d,e). We suggest that these interactions underlie the essential roles of Cdt1 in Mcm2–7 loading on DNA¹³. Cdt1 bound in the OCCM—particularly through its interaction with Mcm2 and the Mcm2–7 subunits that bind ATP (Mcm2, Mcm4, Mcm7, and Mcm3)—may keep the Mcm2–Mcm5 N-tier interface open and prevent Mcm2–7 ATP hydrolysis. ORC–Cdc6 ATPase activity, the next step after OCCM assembly, removes Cdt1 (ref. 30) and may promote Mcm2–7 ATPase activity to close the first Mcm2–7 hexamer^{33,34}.

To further investigate the interactions between Cdt1 and Mcm2–7, we expressed in baculoviruses each Mcm subunit and Cdt1 as Strep–Strep–SUMO–Cdt1 (SSS–Cdt1). Each Mcm subunit alone or all six in combination were expressed, and a pulldown assay with purified SSS–Cdt1 was performed (Supplementary Fig. 8). Cdt1 interacted with all six Mcm proteins when they were expressed together. Individually, Mcm2, Mcm6 (most strongly), and Mcm7 interact with Cdt1. The first two interactions were observed in the OCCM model. We did not see an interaction with Mcm4, which suggests that the Cdt1–CTD interaction with Mcm4 seen in the OCCM structure must depend on prior binding to Mcm2–Mcm6 in the Mcm2–7 hexamer. The interaction with Mcm7 is not present at this stage of OCCM, but it could be functional downstream, when ORC–Cdc6–Mcm2–7 recruits the second Cdt1-bound Mcm2–7 hexamer to form the DH³⁵. Indeed, a long Mcm7 α-helix projects down toward the incoming second Cdt1–Mcm2–7 complex (Fig. 1e).

By comparing the Mcm2–7 in the OCCM with that in the Mcm2–7 DH, we found that Mcm2–7 needed to undergo large conformational changes during the OCCM-to-DH transition, in particular within the entire Mcm2–7 NTD ring as well as in the CTDs of Mcm2 and Mcm5 (Fig. 6 and Supplementary Video 3). Specifically, the Mcm2–7 NTD ring needed to rotate by ~25° relative to the Mcm2–7 CTD to match the MCM ring in the DH, and the CTDs of Mcm2 and Mcm5 had to rotate by ~5° and ~15°, respectively, to form the closed interface in the DH (Fig. 6b,c). Because the ATPase activity of Orc1 and Cdc6 is required during the loading reaction^{29,30,32}, and because Orc1 and Cdc6 appear in a conformation poised to hydrolyze ATP, it is possible

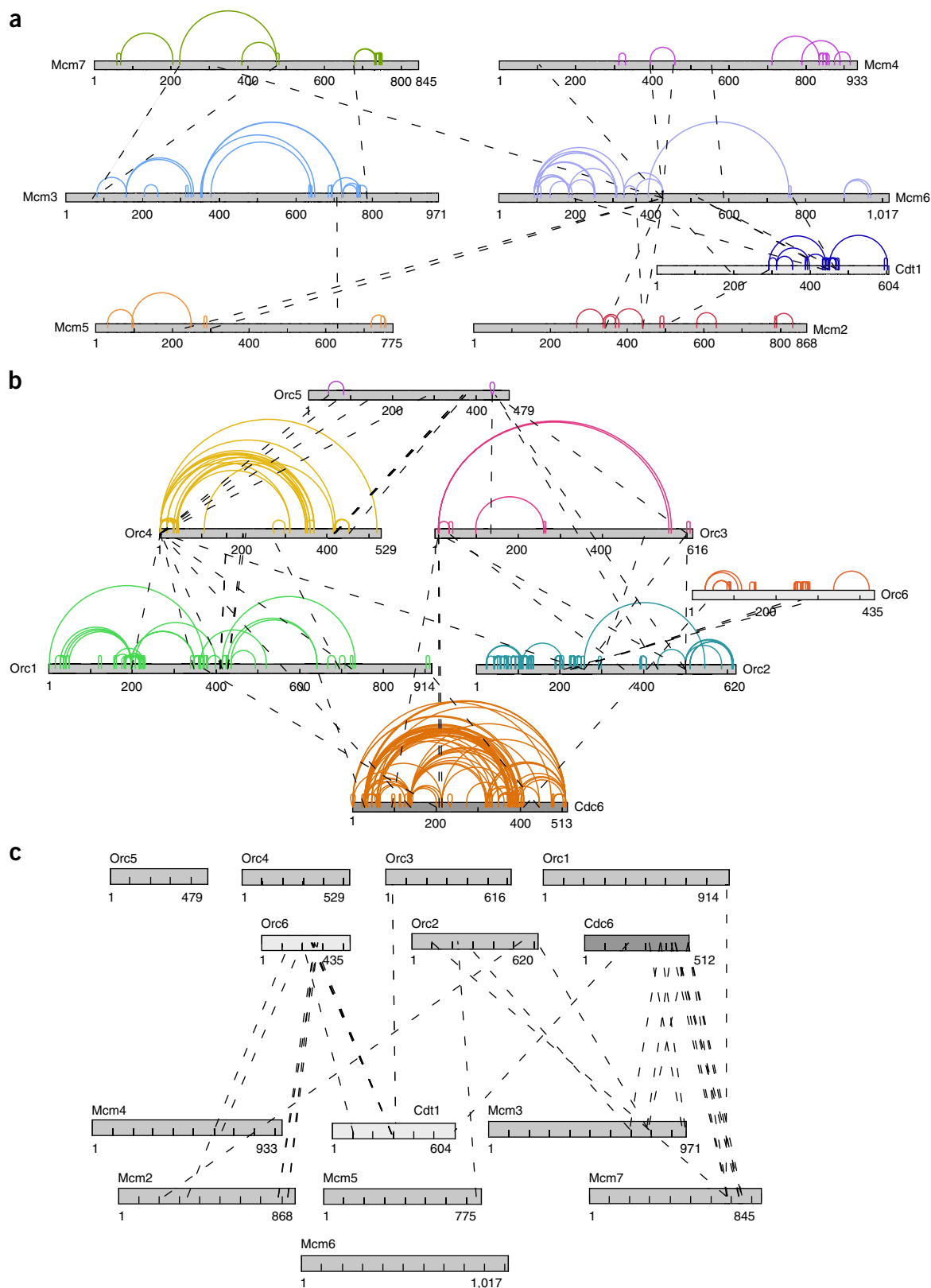


Figure 2 CLMS analysis of the *S. cerevisiae* OCCM complex. **(a)** Linkage map showing the observed cross-linked residue pairs in the Mcm2–7–Cdt1 complex. **(b)** Linkage map showing the observed cross-linked residue pairs in the ORC–Cdc6 complex. **(c)** Linkage map showing the observed cross-linked residue pairs between the ORC–Cdc6 complex and the Mcm2–7–Cdt1 complex. Orc6, which was only partially resolved by cryo-EM, is in close proximity to Mcm2 and Cdt1. The WHD of Mcm5, which was only partially resolved by cryo-EM, is in close proximity to the N-terminal region of Orc2. Intramolecular cross-links are in color, and intermolecular cross-links are indicated by black dashed lines. Source data are provided in **Supplementary Data Set 1**.

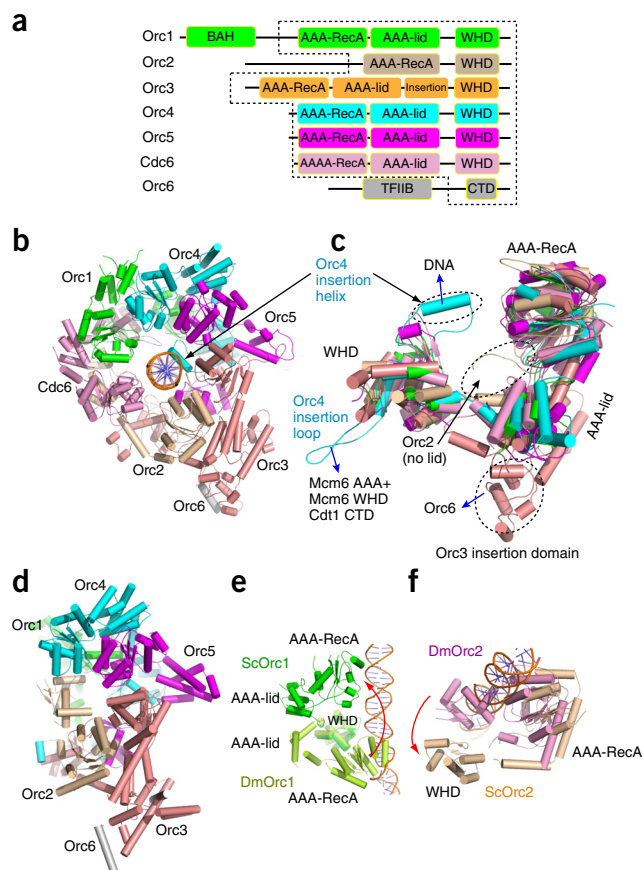


Figure 3 ORC–Cdc6 encircles the origin DNA, and the Orc4 insertion helix binds to the major groove. **(a)** Domain organization of *S. cerevisiae* Orc1–6 subunits and Cdc6. Dashed lines mark the ORC–Cdc6 core regions resolved in our model (TFIIB, transcription factor II-like domain; BAH, bromo-adjacent homology domain). **(b)** The ORC–Cdc6 structure in the *S. cerevisiae* OCCM model (top view). **(c)** Superposition of Orc1–5 and Cdc6, highlighting their similar overall structures. Orc2 lacked the AAA-lid domain, which resulted in a relatively open interface between Orc2 and Cdc6. Orc3 had an insertion domain between the AAA-lid domain and the WHD that interacted with Orc6. The blue arrows point to structures with which these marked elements interact. The black arrow points to the region of the missing lid domain in Orc2. **(d)** Crystal structure of the DmORC. **(e, f)** Alignment of the DmORC with ScORC–Cdc6 (*Sc. S. cerevisiae*), with the most similar Orc3–5 region used as a reference, showed that the AAA–RecA-fold domain of DmOrc1 **(e)** and the WHD of DmOrc2 **(f)** need to move and rotate by 180° to assume their respective positions within ScOCCM. See also **Supplementary Video 1**. Color-coding in **b–f** is mostly as defined in **a**; structures not included in **a** are defined by their color-coded labels.

that the conformational changes outlined here are driven by ORC–Cdc6 ATP hydrolysis. Conceivably, the large conformational changes, which could be mediated by interactions among Orc4, Mcm6, and Cdt1 (**Fig. 5a**), could alter the Cdt1-binding surface, leading to its release from Mcm2–7. As Cdt1 release is known to occur immediately before the recruitment of the second Cdt1-bound Mcm2–7 (refs. 30,32,35), we suggest that ATP hydrolysis by ORC–Cdc6 could facilitate Cdt1 release, thereby completely closing the first Mcm2–7 ring and establishing a condition for the recruitment of the next Cdt1-bound Mcm2–7 hexamer. Alternatively, Mcm ATP hydrolysis could be involved^{33,34}, however, the Mcm2–7 ring is broken in the OCCM, and thus the ATPase activity of Mcm is likely to be blocked at this stage⁴⁵.

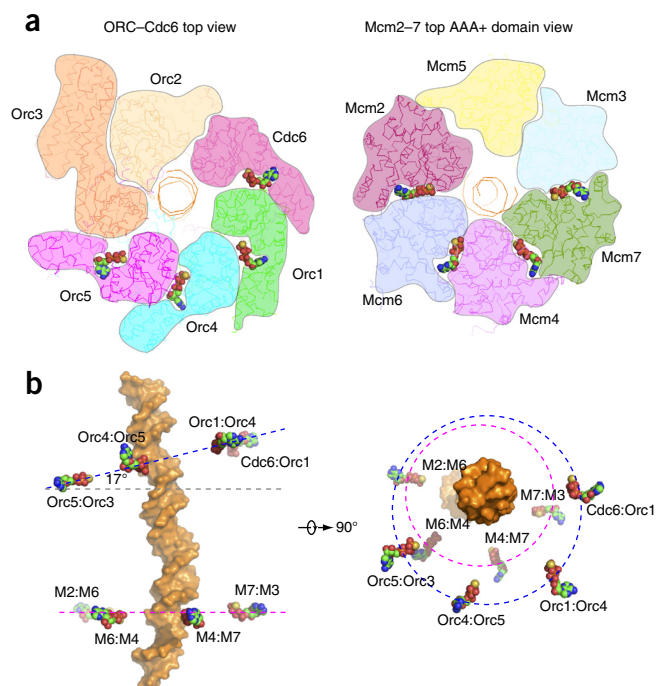


Figure 4 Nucleotide-binding sites and configuration in OCCM. **(a)** Cut-open top view of ORC–Cdc6 and Mcm2–7 shown in surface view. The four ATP γ S molecules identified in ORC–Cdc6 at the Cdc6–Orc1, Orc1–Orc4, Orc4–Orc5, and Orc5–Orc3 interfaces (left) and four ATP γ S molecules in Mcm2–7 at the Mcm2–Mcm6, Mcm6–Mcm4, Mcm4–Mcm7, and Mcm7–Mcm3 interfaces (right) are shown as spheres (carbon in green, oxygen in red, nitrogen in blue, and sulfur in yellow). **(b)** The positions of the observed nucleotides in OCCM depicted relative to the DNA, which is shown in orange in this surface representation. Left, a side view with Mcm4 in front. Right, a top view with ORC–Cdc6 on top. Proteins have been omitted in order to highlight the nucleotides. The four ATP γ S molecules in ORC–Cdc6 are coplanar, but the plane is tilted by $\sim 17^\circ$ with respect to the plane formed by the nucleotides in Mcm2–7. An imaginary circle defined by the nucleotide in ORC–Cdc6 is larger (75 Å; blue dashed lines) than the circle defined by nucleotides in Mcm2–7 (65 Å; pink dashed lines), and the two circles are acentric. M, Mcm.

Asymmetric interaction between ORC–Cdc6 and Cdt1–Mcm2–7 enables DNA insertion

Although both the Mcm2–7 hexamer and ORC–Cdc6 form ring-like structures with a pseudo-six-fold symmetry, the interaction between the two rings is asymmetrical owing to the $\sim 17^\circ$ tilt of the ORC–Cdc6 ring with respect to the Mcm2–7 ring (**Figs. 1d** and **4**). As a consequence, the DNA is bent by ~ 20 – 25° at the interface. Furthermore, the tilt leads to a tight interface between Orc1–Orc4–Orc5 and Mcm4–Mcm6–Mcm2, and an apparent ‘loose’ interface between Orc3–Orc2–Cdc6 and Mcm5–Mcm3–Mcm7. At the tight interface, the WHDs of Orc1 and Orc4 insert into the gaps between the WHDs and the AAA-lid domains of Mcm4 and Mcm6; the Orc5 WHD interacts only with the Mcm2 AAA–RecA-fold, because Mcm2 lacks a WHD (**Fig. 1d, e** and **Supplementary Fig. 7**). At the loose interface, the WHD of Mcm5 was not visible in the EM map, but the CLMS data identified it as the across-the-interface partner of Orc2. Interestingly, the WHDs of Mcm3 and Mcm7 reached upward more than 30 Å via their long loops to interact with Orc2 and Cdc6, respectively (**Fig. 1e** and **Supplementary Fig. 7**). Accordingly, we propose that the asymmetric interaction leaves half of the Mcm2–7 ring (Mcm5–Mcm3–Mcm7) only loosely tethered, such that the Mcm5–Mcm3–Mcm7 half-ring

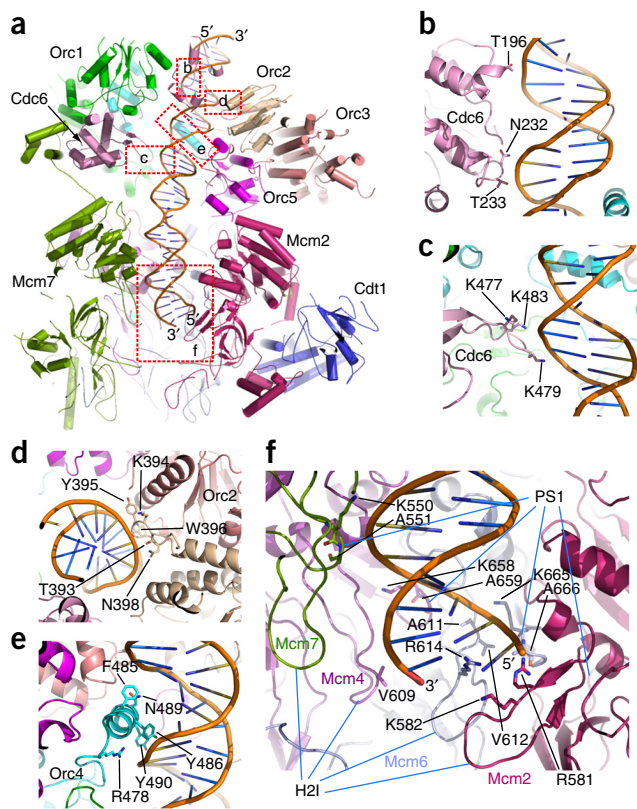


Figure 7 Interactions between OCCM and DNA. (a) An overview of the OCCM–DNA structure in side view. Subunits in front of DNA, including parts of Orc1 and Cdc6 and all of Mcm3 and Mcm5, have been omitted to make the DNA visible. The five areas framed by red dashed rectangles are enlarged in c–f, as indicated. (b–e) Detailed view of dsDNA interactions of Cdc6 (b,c), Orc2 (d), and Orc4 (e) subunits. (f) DNA interfaces with Mcm2, Mcm6, Mcm4, and Mcm7. PS1, presensor 1 β -hairpin loop; H2I, helix-2-insert β -hairpin loop.

(Supplementary Fig. 10). It is possible that DNA bends and binds to some of these surfaces in addition to the central channel.

In the lower Cdt1–Mcm2–7 region, Mcm3 and Mcm5 did not interact with DNA. Although the Mcm2–7 ring was nearly flat, the hairpin loops in the AAA+ domains of Mcm2–Mcm4–Mcm6–Mcm7 were arranged in a spiral to grip the DNA (Fig. 7a,f). We found that Mcm2, Mcm4, and Mcm6 interacted with DNA via their respective helix-2-insert (H2I) β -hairpin loops. Mcm4, Mcm6, and Mcm7 contacted the DNA with their respective presensor 1 (PS1) β -hairpin loops, in particular the well-conserved KA motifs (Fig. 7f and Supplementary Fig. 9). In contrast, the same H2I and PS1 within the Mcm2–7 DH are involved in intersubunit interactions¹⁴. In the apo form of the active CMG helicase, the PS1 loops face the central DNA channel⁵³, and in a recent cryo-EM structure of CMG at sub-nanometer resolution, the PS1 loops were found to interact with a six-base single-stranded DNA⁵⁴. Interestingly, most of these hairpin loops, except for the Mcm4 H2I loop, interacted with the same strand of the duplex DNA (Fig. 7f). It is unclear whether this strand functions as the leading or the lagging strand in the CMG helicase, because extensive conformation changes must occur in Mcm2–7 in order for the active helicase to form, such that Mcm–DNA interaction in the CMG may be very different.

DISCUSSION

Since the discovery of ORC more than two decades ago², a key issue in the DNA-replication field has been the question of how ORC

recognizes dsDNA and cooperates with Cdc6 to load the Mcm2–7 hexamers onto DNA. The current atomic model of the OCCM provides the first high-resolution structure of ORC–Cdc6 bound to origin DNA. Overall, the ORC–Cdc6 structure is flat, but within the structure the subunits that bind ATP, Orc1, Orc4, Orc5, and Cdc6 form a right-handed spiral around the dsDNA, similar to the spiral of AAA+ subunits around primer–template DNA in RFC clamp loaders^{49,50}. The human ORC has an almost identical structure (A. Tocilj, K. On, Z. Yuan, J. Sun, E. Elkayam, H. Li, B. Stillman and L. Joshua-Tor, submitted manuscript). Orc4 has an unusual insertion α -helix that appears to contact the major groove of the dsDNA. This helix is unique to budding yeast Orc4 subunits, being absent in the DmORC and human ORC4 structures⁷ (A. Tocilj, K. On, Z. Yuan, J. Sun, E. Elkayam, H. Li, B. Stillman and L. Joshua-Tor, submitted manuscript), and it may help to explain the sequence specificity of ORC that is characteristic of origin binding in *Saccharomyces* spp. Cdc6 is particularly important for DNA binding with two principal DNA-binding sites, the ISM and the WHD, which explains why Cdc6 enhances the ORC's specificity for DNA^{9,10}.

The most prominent feature of Mcm2–7 loading by ORC–Cdc6 is the extensive use of WHDs of these replication proteins. There were six resolved WHDs in ORC–Cdc6 that formed a larger winged-helix ring in the upper tier of the OCCM, and five cryo-EM- and CLMS-resolved WHDs in Mcm2–7 that formed a second slightly smaller winged-helix ring on the lower Mcm2–7 tier of the OCCM. This appears to be an evolutionarily conserved interaction, as it was reported recently for archaeal MCM and Orc1 (ref. 55). However, here we observed that the WHD-mediated correct stacking of the two rings mediated much of the recruitment mechanism. The position of the WHD of the Mcm proteins varies widely: it can sit right above the AAA+ domain, or move away from the main body of the protein, or even move to the side of the AAA+ domain in the case of Mcm5, as seen in the active helicase (Supplementary Fig. 7). The CTD of Cdt1 has a special role in displacing the Mcm6 WHD to create the ORC–Cdc6 binding surface; we showed previously that the WHD of Mcm6 is inhibitory and blocks OCCM formation in the absence of Cdt1 (ref. 32). The attachment of the WHDs by flexible linker provides these domains with manifold potential to interact with ORC–Cdc6, but after helicase activation they could also be important interaction partners with other proteins at the DNA replication fork.

The Mcm2–7 DH structure, although obtained in the absence of DNA, showed that six H2I hairpin loops are arranged in an approximately helical trajectory that was suggested to facilitate DNA translocation and unwinding. However, in the OCCM, only three H2I hairpin loops of Mcm2–Mcm4–Mcm6 contact DNA. In addition, the three PS1 hairpin loops of Mcm4, Mcm6, and Mcm7 make contact with DNA. In the DH, the PS1 loop is involved in intersubunit interaction, not in DNA binding, but in the CMG helicase, the PS1 loop contacts DNA^{14,54}. Another interesting feature of the OCCM is the partially open Mcm2–Mcm5 interface. Thus the data provide the first structural proof that the Mcm2–Mcm5 interface is the DNA entry gate in Mcm2–7 during pre-RC formation^{22,31,43}. ATP γ S prevents Cdt1 removal and stops the gate from closing^{30,32}, and thus it is interesting that the N-tier ring was not yet closed in our structure, given that the dsDNA had been loaded into the Mcm2–7 hexamer channel. We suggest that Mcm2–7 N-tier ring closure requires ATP hydrolysis by Orc1 and Cdc6 and removal of Cdt1 from the Mcm2–7 hexamer. The unusually extended three-domain structure of Cdt1 probably keeps Mcm2–7 subunits vertically aligned, preventing the left-handed spiral of the Mcm2–7 subunits in the completely assembled Mcm2–7 DH (Fig. 6c). Thus, like the RFC–PCNA clamp loader and clamp structures, the OCCM structure provides further insight into how an

AAA+ complex loads a ring-shaped, multisubunit complex of proteins around dsDNA to promote DNA replication. We suggest that ORC–Cdc6 ATPase promotes complete Mcm2–7 ring closure just as ATP hydrolysis by the clamp loader RFC locks the PCNA DNA polymerase clamp onto dsDNA⁵⁰.

METHODS

Methods, including statements of data availability and any associated accession codes and references, are available in the [online version of the paper](#).

Note: Any Supplementary Information and Source Data files are available in the [online version of the paper](#).

ACKNOWLEDGMENTS

Cryo-EM data were collected on a FEI Titan Krios at HHMI Janelia Farm. We also collected a cryo-EM data set on an FEI Technai F20 equipped with a K2 detector at NRAMM at the Scripps Research Institute, which is supported by NIH grant P41 GM103310. We thank Z. Yu, C. Hong, and R. Huang at HHMI, and C. Porter and B. Carragher at Scripps for help with data collection. H.L. dedicates this work to the loving memory of his son Paul J. Li. This work was funded by the US National Institutes of Health (grant GM111742 to H.L., and grant GM45436 to B.S.), the Biotechnology and Biological Sciences Research Council UK (grant P56061 to C. Speck), and the Wellcome Trust (Investigator Award P56628 to C. Speck, Senior Research Fellowship 103139 to J.R., Centre core grant 092076 to J.R., and instrument grant 108504 to J.R.).

AUTHOR CONTRIBUTIONS

Z.Y., A.R., L.B., J.S., J.R., Z.A.C., B.S., C. Speck, and H.L. designed experiments. Z.Y., A.R., L.B., S.N., C. Spanos, M.B., and J.S. performed experiments. Z.Y., A.R., L.B., J.S., Z.A.C., J.R., B.S., C. Speck, and H.L. analyzed the data. L.B., B.S., C. Speck, and H.L. wrote the manuscript with input from all other authors.

COMPETING FINANCIAL INTERESTS

The authors declare no competing financial interests.

Reprints and permissions information is available online at <http://www.nature.com/reprints/index.html>.

- Bell, S.P. & Dutta, A. DNA replication in eukaryotic cells. *Annu. Rev. Biochem.* **71**, 333–374 (2002).
- Bell, S.P. & Stillman, B. ATP-dependent recognition of eukaryotic origins of DNA replication by a multiprotein complex. *Nature* **357**, 128–134 (1992).
- Stillman, B. Origin recognition and the chromosome cycle. *FEBS Lett.* **579**, 877–884 (2005).
- Li, H. & Stillman, B. The origin recognition complex: a biochemical and structural view. *Subcell. Biochem.* **62**, 37–58 (2012).
- Chen, Z. *et al.* The architecture of the DNA replication origin recognition complex in *Saccharomyces cerevisiae*. *Proc. Natl. Acad. Sci. USA* **105**, 10326–10331 (2008).
- Sun, J. *et al.* Cdc6-induced conformational changes in ORC bound to origin DNA revealed by cryo-electron microscopy. *Structure* **20**, 534–544 (2012).
- Bleichert, F., Botchan, M.R. & Berger, J.M. Crystal structure of the eukaryotic origin recognition complex. *Nature* **519**, 321–326 (2015).
- Bell, S.P. & Labib, K. Chromosome duplication in *Saccharomyces cerevisiae*. *Genetics* **203**, 1027–1067 (2016).
- Speck, C., Chen, Z., Li, H. & Stillman, B. ATPase-dependent cooperative binding of ORC and Cdc6 to origin DNA. *Nat. Struct. Mol. Biol.* **12**, 965–971 (2005).
- Speck, C. & Stillman, B. Cdc6 ATPase activity regulates ORC × Cdc6 stability and the selection of specific DNA sequences as origins of DNA replication. *J. Biol. Chem.* **282**, 11705–11714 (2007).
- Cocker, J.H., Piatti, S., Santocanale, C., Nasmyth, K. & Diffley, J.F. An essential role for the Cdc6 protein in forming the pre-replicative complexes of budding yeast. *Nature* **379**, 180–182 (1996).
- Evrin, C. *et al.* A double-hexameric MCM2–7 complex is loaded onto origin DNA during licensing of eukaryotic DNA replication. *Proc. Natl. Acad. Sci. USA* **106**, 20240–20245 (2009).
- Remus, D. *et al.* Concerted loading of Mcm2–7 double hexamers around DNA during DNA replication origin licensing. *Cell* **139**, 719–730 (2009).
- Li, N. *et al.* Structure of the eukaryotic MCM complex at 3.8 Å. *Nature* **524**, 186–191 (2015).
- Sun, J. *et al.* Structural and mechanistic insights into Mcm2–7 double-hexamer assembly and function. *Genes Dev.* **28**, 2291–2303 (2014).
- Moyer, S.E., Lewis, P.W. & Botchan, M.R. Isolation of the Cdc45/Mcm2–7/GINS (CMG) complex, a candidate for the eukaryotic DNA replication fork helicase. *Proc. Natl. Acad. Sci. USA* **103**, 10236–10241 (2006).
- Gambus, A. *et al.* GINS maintains association of Cdc45 with MCM in replisome progression complexes at eukaryotic DNA replication forks. *Nat. Cell Biol.* **8**, 358–366 (2006).
- Remus, D. & Diffley, J.F. Eukaryotic DNA replication control: lock and load, then fire. *Curr. Opin. Cell Biol.* **21**, 771–777 (2009).
- Yardimci, H., Loveland, A.B., Habuchi, S., van Oijen, A.M. & Walter, J.C. Uncoupling of sister replisomes during eukaryotic DNA replication. *Mol. Cell* **40**, 834–840 (2010).
- Botchan, M. & Berger, J. DNA replication: making two forks from one prereplication complex. *Mol. Cell* **40**, 860–861 (2010).
- Aparicio, T., Guillo, E., Coloma, J., Montoya, G. & Méndez, J. The human GINS complex associates with Cdc45 and MCM and is essential for DNA replication. *Nucleic Acids Res.* **37**, 2087–2095 (2009).
- Costa, A. *et al.* The structural basis for MCM2–7 helicase activation by GINS and Cdc45. *Nat. Struct. Mol. Biol.* **18**, 471–477 (2011).
- Zegerman, P. & Diffley, J.F. Phosphorylation of Sld2 and Sld3 by cyclin-dependent kinases promotes DNA replication in budding yeast. *Nature* **445**, 281–285 (2007).
- Araki, H. Cyclin-dependent kinase-dependent initiation of chromosomal DNA replication. *Curr. Opin. Cell Biol.* **22**, 766–771 (2010).
- Sheu, Y.J. & Stillman, B. The Dbf4-Cdc7 kinase promotes S phase by alleviating an inhibitory activity in Mcm4. *Nature* **463**, 113–117 (2010).
- Deegan, T.D., Yeeles, J.T. & Diffley, J.F. Phosphopeptide binding by Sld3 links Dbf4-dependent kinase to MCM replicative helicase activation. *EMBO J.* **35**, 961–973 (2016).
- O'Donnell, M., Langston, L. & Stillman, B. Principles and concepts of DNA replication in bacteria, archaea, and eukarya. *Cold Spring Harb. Perspect. Biol.* **5**, a010108 (2013).
- Yeeles, J.T., Deegan, T.D., Janska, A., Early, A. & Diffley, J.F. Regulated eukaryotic DNA replication origin firing with purified proteins. *Nature* **519**, 431–435 (2015).
- Evrin, C. *et al.* In the absence of ATPase activity, pre-RC formation is blocked prior to MCM2–7 hexamer dimerization. *Nucleic Acids Res.* **41**, 3162–3172 (2013).
- Ticau, S., Friedman, L.J., Ivica, N.A., Gelles, J. & Bell, S.P. Single-molecule studies of origin licensing reveal mechanisms ensuring bidirectional helicase loading. *Cell* **161**, 513–525 (2015).
- Samel, S.A. *et al.* A unique DNA entry gate serves for regulated loading of the eukaryotic replicative helicase MCM2–7 onto DNA. *Genes Dev.* **28**, 1653–1666 (2014).
- Fernández-Cid, A. *et al.* An ORC/Cdc6/MCM2–7 complex is formed in a multistep reaction to serve as a platform for MCM double-hexamer assembly. *Mol. Cell* **50**, 577–588 (2013).
- Kang, S., Warner, M.D. & Bell, S.P. Multiple functions for Mcm2–7 ATPase motifs during replication initiation. *Mol. Cell* **55**, 655–665 (2014).
- Coster, G., Frigola, J., Beuron, F., Morris, E.P. & Diffley, J.F. Origin licensing requires ATP binding and hydrolysis by the MCM replicative helicase. *Mol. Cell* **55**, 666–677 (2014).
- Evrin, C. *et al.* The ORC/Cdc6/MCM2–7 complex facilitates MCM2–7 dimerization during prereplicative complex formation. *Nucleic Acids Res.* **42**, 2257–2269 (2014).
- Chang, F. *et al.* Cdc6 ATPase activity disengages Cdc6 from the pre-replicative complex to promote DNA replication. *eLife* **4**, e05795 (2015).
- Bleichert, F. *et al.* A Meier-Gorlin syndrome mutation in a conserved C-terminal helix of Orc6 impedes origin recognition complex formation. *eLife* **2**, e00882 (2013).
- Balaso, M., Akhmetova, K. & Chesnokov, I. *Drosophila* model of Meier-Gorlin syndrome based on the mutation in a conserved C-terminal domain of Orc6. *Am. J. Med. Genet. A.* **167A**, 2533–2540 (2015).
- Gaudier, M., Schuwirth, B.S., Westcott, S.L. & Wigley, D.B. Structural basis of DNA replication origin recognition by an ORC protein. *Science* **317**, 1213–1216 (2007).
- Liu, C. *et al.* Structural insights into the Cdt1-mediated MCM2–7 chromatin loading. *Nucleic Acids Res.* **40**, 3208–3217 (2012).
- Wei, Z. *et al.* Characterization and structure determination of the Cdt1 binding domain of human minichromosome maintenance (Mcm) 6. *J. Biol. Chem.* **285**, 12469–12473 (2010).
- Lee, C. *et al.* Structural basis for inhibition of the replication licensing factor Cdt1 by geminin. *Nature* **430**, 913–917 (2004).
- Bochman, M.L. & Schwacha, A. The Mcm2–7 complex has in vitro helicase activity. *Mol. Cell* **31**, 287–293 (2008).
- Sun, J. *et al.* Cryo-EM structure of a helicase loading intermediate containing ORC–Cdc6–Cdt1–MCM2–7 bound to DNA. *Nat. Struct. Mol. Biol.* **20**, 944–951 (2013).
- Enemark, E.J. & Joshua-Tor, L. On helicases and other motor proteins. *Curr. Opin. Struct. Biol.* **18**, 243–257 (2008).
- Neuwald, A.F., Aravind, L., Spouge, J.L. & Koonin, E.V. AAA+: a class of chaperone-like ATPases associated with the assembly, operation, and disassembly of protein complexes. *Genome Res.* **9**, 27–43 (1999).
- Bowers, J.L., Randall, J.C., Chen, S. & Bell, S.P. ATP hydrolysis by ORC catalyzes reiterative Mcm2–7 assembly at a defined origin of replication. *Mol. Cell* **16**, 967–978 (2004).
- Frigola, J., Remus, D., Mehanna, A. & Diffley, J.F. ATPase-dependent quality control of DNA replication origin licensing. *Nature* **495**, 339–343 (2013).

49. O'Donnell, M. & Kuriyan, J. Clamp loaders and replication initiation. *Curr. Opin. Struct. Biol.* **16**, 35–41 (2006).
50. Kelch, B.A., Makino, D.L., O'Donnell, M. & Kuriyan, J. How a DNA polymerase clamp loader opens a sliding clamp. *Science* **334**, 1675–1680 (2011).
51. Dueber, E.L.C., Corn, J.E., Bell, S.D. & Berger, J.M. Replication origin recognition and deformation by a heterodimeric archaeal Orc1 complex. *Science* **317**, 1210–1213 (2007).
52. Suck, D. & Oefner, C. Structure of DNase I at 2.0 Å resolution suggests a mechanism for binding to and cutting DNA. *Nature* **321**, 620–625 (1986).
53. Yuan, Z. *et al.* Structure of the eukaryotic replicative CMG helicase suggests a pumpjack motion for translocation. *Nat. Struct. Mol. Biol.* **23**, 217–224 (2016).
54. Abid Ali, F. *et al.* Cryo-EM structures of the eukaryotic replicative helicase bound to a translocation substrate. *Nat. Commun.* **7**, 10708 (2016).
55. Samson, R.Y., Abeyrathne, P.D. & Bell, S.D. Mechanism of archaeal MCM helicase recruitment to DNA replication origins. *Mol. Cell* **61**, 287–296 (2016).

ONLINE METHODS

Sample preparation and electron microscopy. The *S. cerevisiae* loading intermediate OCCM was assembled *in vitro* with purified ORC, Cdc6, Cdt1, and Mcm2–7 on plasmid DNA containing the ARS1 sequence in the presence of ATP γ S, and isolated via a previously described⁴⁴ magnetic bead pulldown approach, with minor modifications. Twenty-four pre-RC reactions containing 40 nM ORC, 80 nM Cdc6, 40 nM Cdt1, 40 nM MCM2–7 and 6 nM pUC19-ARS1 beads in 50 μ l of buffer A (50 mM HEPES-KOH, pH 7.5, 100 mM potassium glutamate, 10 mM magnesium acetate, 50 μ M zinc acetate, 3 mM ATP γ S, 5 mM DTT, 0.1% Triton X-100 and 5% glycerol) were incubated for 15 min at 24 °C. After three washes with buffer B (50 mM HEPES-KOH, pH 7.5, 100 mM K acetate, 3 mM ATP γ S) the complex was eluted with 1 U of DNase I in buffer B and 1 mM CaCl₂.

To prepare cryo-EM grids, we pooled all the elutions together and concentrated the sample to about 0.9 mg/ml in buffer B with a Microcon centrifugal filter unit (YM-100 membrane). Before preparing the EM grid, we checked the sample for homogeneity by negative-stain EM. We then applied 3 μ l of OCCM sample at a final concentration of 0.9 mg/ml to glow-discharged C-flat 1.2/1/3 holey carbon grids, incubated the grids for 10 s at 6 °C and 95% humidity, blotted the grids for 3 s, and plunged the grids into liquid ethane using an FEI Vitrobot IV. We loaded the grids into an FEI Titan Krios electron microscope operated at 300 kV high tension and collected images semi-automatically with SerialEM under low-dose mode at a magnification of 29,000 \times and a pixel size of 1.01 Å per pixel. A Gatan K2 summit direct electron detector was used under super-resolution mode for image recording with an under-focus range from 1.5 to 3.5 μ m. The dose rate was 10 electrons per Å² per second, and the total exposure time was 5 s. The total dose was divided into a 25-frame movie, and each frame was exposed for 0.2 s.

Image processing and 3D reconstruction. Approximately 7,500 raw movie micrographs were collected. The movie frames were first aligned and superimposed by the program MotionCorr⁵⁶. Contrast transfer function parameters of each aligned micrograph were calculated using the program CTFIND4 (ref. 57). All the remaining steps, including particle auto-selection, 2D classification, 3D classification, 3D refinement, and density map post-processing, were done with Relion-1.4 (ref. 58). We manually picked ~10,000 particles from different views to generate 2D averages, which we used as templates for subsequent automatic particle selection. Automatic particle selection was then carried out for the entire data set. First we selected 1,371,667 particles. Then we carefully checked the particles obtained from automatic picking, removed the bad particles, and re-picked the missing good ones. Particles were then sorted by similarity to the 2D references; the 10% of particles with the lowest *z* scores were deleted from the particle pool. 2D classification of all remaining particles was performed, and particles in unrecognizable classes by visual inspection were removed. A total of 601,095 particles were used for 3D classification. We derived six 3D models from the data set, and we found that two models were similar to each other. The associated particles from those two models were combined for further refinement; the other four models were distorted, and their particles were discarded, which led to a data set that included 304,288 particles. This final data set was used for further 3D refinement, which resulted in the 3.91-Å 3D density map. We estimated the resolution of the map by using the so-called gold-standard Fourier shell correlation, at the correlation cutoff value of 0.143. We correlated the 3D density maps for the detector modulation transfer function and sharpened them by applying a negative *B* factor of –112 Å². The particles had some preference for end-on views, but because of the large number of particles used, virtually all of the angular space was sampled.

Structural modeling, refinement, and validation. The yeast Mcm2–7 models were directly extracted from the cryo-EM structure of the yeast Mcm2–7 DH (PDB 3JA8)¹⁴. For subsequent docking, each Mcm protein was split into two parts: the NTD and the CTD. The initial models of the *S. cerevisiae* Orc1–5 subunits were generated from the crystal structure of the *Drosophila* ORC complex (PDB 4XGC)⁷, and the Cdc6 subunit was generated from the homolog Archaeal structure (PDB 2V1U)³⁹, using the SWISS-MODEL server⁵⁹. These models were first docked and fitted into the density map using COOT⁶⁰ and Chimera⁶¹. We found that Orc1 and Orc2 in the yeast OCCM had gone through dramatic conformational changes compared with the fly ORC structure. Thus, we split each of the two proteins into three parts—the AAA-RecA fold, the AAA-lid domain (where

present), and the C-terminal WHD—and fitted these domains independently into the 3D density map. The structural features showed that the extra density outside Mcm2 and Mcm6 clearly belonged to the NTD and the MHD of Cdt1 (ref. 44). We used the SWISS-MODEL server to generate the atomic models of the Cdt1 NTD and MHD from their respective homologous structures (PDB 5C3P and PDB 2ZXX)^{42,62}. The Cdt1 CTD model was generated from the human Cdt1 crystal structure (PDB 2WVR)⁶³, and this domain was found in the region between Mcm6 and Mcm4. Four bulky densities outside the core structure of Cdc6–ORC were identified as the WHDs of Mcm3, Mcm4, Mcm6, and Mcm7, respectively. We generated their atomic models from their corresponding homolog structures (PDB 3NW0, PDB 2M45, PDB 2KLQ, and PDB 2OD5)^{41,64,65} using the SWISS-MODEL server. The Orc6 density was very weak, indicating high flexibility of this protein. However, on the basis of the homologous *Drosophila* ORC core complex structure (PDB 4XGC)⁷, we identified a short α -helix at the C terminus of Orc6 that bound to and was stabilized by Orc3. The dsDNA was built into the long helical density that ran through the OCCM structure in the program COOT. The entire OCCM atomic model was subsequently adjusted manually and rebuilt in COOT. Clearly resolved bulky residues such as Phe, Tyr, Trp, and Arg were used for sequence registration.

The manually built atomic model was then iteratively refined in real space by phenix.real_space_refine⁶⁶ and rebuilt in COOT. We also performed the reciprocal space-refinement procedure with the application of secondary structure and stereochemical constraints in the program Phenix⁶⁷. We calculated the structure factors (including phases) by Fourier transform of the experimental density map with the program Phenix.map_to_structure_factors. We validated the atomic model by using MolProbity⁶⁸. Structural figures were prepared in Chimera and Pymol (<https://www.pymol.org>).

We cross-validated the final model by using a previously described method⁶⁹. Briefly, we randomly added 0.1 Å noise to the coordinates of the final model by using the PDB tools in Phenix, and then we refined the noise-added model against the first half-map (Half1) that was produced from one half of the particle data set during refinement by RELION. We performed one round of coordinate refinement followed by a *B*-factor refinement. The refined model was then correlated with the 3D maps of the two half-maps (Half1 and Half2) in Fourier space to produce two FSC curves: FSC_{work} (model versus Half1 map) and FSC_{free} (model versus Half2 map). A third FSC curve was calculated between the refined model and the final 3.9-Å-resolution density map produced from all particles. The general agreement of these curves was taken as an indication that the model was not overfitted.

Cross-linking/mass spectrometry analysis. We used 240 nM pUC19-ARS1 beads to assemble the OCCM complex as previously described¹². The complex was cross-linked in the presence of the beads with BS3 1:8,100 (molar protein: cross-linker ratio) for 2 h at 4 °C. Then the reaction was quenched with 50 μ l of saturated ammonium bicarbonate for 45 min at 4 °C and subsequently transferred into digestion buffer (50 mM ammonium bicarbonate, 8 M urea). Next the reaction was subjected to reduction with DTT and alkylation with iodoacetamide. We added 3 μ g of LysC (with an estimated 1:50 enzyme-to-protein ratio) and incubated it at room temperature for 4 h. The digestion buffer was then diluted with 50 mM ammonium bicarbonate to a final urea concentration of 2 M. We added 3 μ g of trypsin (at an estimated 1:50 enzyme-to-protein ratio) and incubated it for 16 h at room temperature. After digestion, the supernatant was collected and acidified using 200 μ l of 10% trifluoroacetic acid. The peptide mixture was then desalted using C18 StageTips for mass spectrometric analysis⁷⁰. We carried out LC-MS/MS analysis on an Orbitrap Fusion Lumos Tribrid mass spectrometer (Thermo Scientific), applying a ‘high-high’ acquisition strategy⁷¹. We injected 2 μ g of peptide mixture for each mass spectrometric acquisition. Peptides were separated on a 50-cm EASY-Spray column (Thermo Scientific) assembled in an EASY-Spray source (Thermo Scientific), operated at a column temperature of 50 °C. Mobile phase A consisted of water, 0.1% (v/v) formic acid, and 5% (v/v) DMSO. Mobile phase B consisted of 80% (v/v) acetonitrile, 0.1% (v/v) formic acid, and 5% (v/v) DMSO. Peptides were loaded at a flow rate of 0.3 μ l/min and eluted at 0.2 μ l/min with a linear gradient from 2% mobile phase B to 40% mobile phase B over 139 min, followed by a linear increase from 45% to 95% mobile phase B in 12 min. The eluted peptides were directly introduced into the mass spectrometer. MS data were acquired in the data-dependent mode with the top-speed option. For each 3-s acquisition cycle, the mass

spectrum was recorded in the Orbitrap with a resolution of 120,000. The ions with a precursor charge state between 3+ and 8+ were isolated and fragmented. The fragmentation spectra were then recorded in the Orbitrap. Dynamic exclusion was enabled with single repeat count and 60-s exclusion duration. To improve the identification of cross-linked peptides, were carried out nine acquisitions in total, with parameter variations mainly related to criteria for ion selection for fragmentation and fragmentation methods.

Identification of cross-linked peptides. The raw mass spectrometric data files were processed into peak lists with MaxQuant version 1.5.2.8 (ref. 72) with the default parameters, except that “FTMS top peaks per 100 Da” was set to 20 and “FTMS de-isotoping” was disabled. The peak lists were searched against the sequences as well as the reversed sequences (as decoys) of 14 OCCM subunits using Xi software (ERI, Edinburgh) for the identification of cross-linked peptides. The search parameters were as follows: MS accuracy, 6 p.p.m.; MS2 accuracy, 20 p.p.m.; enzyme, trypsin; specificity, fully tryptic; allowed number of missed cleavages, four; cross-linker, BS3; fixed modifications, carbamidomethylation on cysteine; variable modifications, oxidation on methionine, and modifications by BS3 that are hydrolyzed or amidated on the other end. The reaction specificity for BS3 was assumed to be for lysine, serine, threonine, tyrosine, and protein N termini. For acquisitions where collision-induced dissociation and higher-energy collisional dissociation fragmentations were applied (acquisitions 1, 3, 4, 6, 7, and 9), only b- and y-ions were considered for the fragment ion matches; for data acquired using combined fragmentation by electron-transfer dissociation supplemented with collision-induced dissociation or higher-energy collisional dissociation (acquisitions 2, 5, and 8), b-, y-, c-, and z-ions were considered for fragment ion matches. Two independent quality control approaches were applied for identified cross-linked peptide candidates. All cross-linked peptides with an estimated 5% false discovery rate at the residue-pair level were accepted for further structural interpretation. We also accepted cross-linked peptides identified with MS2 spectra that passed machine-learning-based auto-validation.

In vitro pulldown of Cdt1 with Mcm2–7 proteins. Baculoviruses expressing Mcm2–7 subunits (Mcm3 was tagged with hemagglutinin at the N terminus) and SSS–Cdt1 were prepared in the Profold-C1 expression vector (AB Vector, San Diego, California). We infected 2.5×10^7 Hi-Five insect cells at a multiplicity of infection of 10 with each Mcm subunit alone or in combination with SSS–Cdt1, and harvested them at 55 h post-infection. After the cells had been washed in cold PBS, they were placed for 10 min on ice in <1 ml of hypotonic buffer (25 mM Hepes-KOH, pH 7.5, 20 mM K glutamate, 1 mM Mg acetate, 1 mM DTT, 5 mM ATP, protease inhibitor (Roche, 1 tablet in 50 ml)). Cell extracts were prepared by Dounce B homogenization and centrifugal clarification (10,000 r.p.m. in a Sorvall SS34 rotor) at 4 °C, and then 100 µl of supernatant was incubated for 2 h on ice with 50 µl of Strep-Tactin sepharose (IBA) that had previously been washed

in PBS and hypotonic buffer. Beads were washed (three times, 5 min) with IP buffer (25 mM Hepes-KOH, pH 7.5, 300 mM K glutamate, 10 mM Mg acetate, 0.04% NP-40, 1 mM DTT, 5 mM ATP, and protease inhibitor). Bead-bound proteins were run on an SDS-PAGE gel and stained with silver.

Data availability. The 3D cryo-EM map of OCCM at 3.9-Å resolution has been deposited at the EMDB database with accession code [EMD-8540](#). The corresponding atomic model was deposited at the RCSB PDB with accession code [5UDB](#). Source data for [Figure 2](#) and [Supplementary Figure 4](#) are available with the paper online.

56. Li, X. *et al.* Electron counting and beam-induced motion correction enable near-atomic-resolution single-particle cryo-EM. *Nat. Methods* **10**, 584–590 (2013).
57. Rohou, A. & Grigorieff, N. CTFIND4: fast and accurate defocus estimation from electron micrographs. *J. Struct. Biol.* **192**, 216–221 (2015).
58. Scheres, S.H. Semi-automated selection of cryo-EM particles in RELION-1.3. *J. Struct. Biol.* **189**, 114–122 (2015).
59. Biasini, M. *et al.* SWISS-MODEL: modelling protein tertiary and quaternary structure using evolutionary information. *Nucleic Acids Res.* **42**, W252–W258 (2014).
60. Emsley, P. & Cowtan, K. Coot: model-building tools for molecular graphics. *Acta Crystallogr. D Biol. Crystallogr.* **60**, 2126–2132 (2004).
61. Pettersen, E.F. *et al.* UCSF Chimera—a visualization system for exploratory research and analysis. *J. Comput. Chem.* **25**, 1605–1612 (2004).
62. Li, W., Zhang, T. & Ding, J. Molecular basis for the substrate specificity and catalytic mechanism of thymine-7-hydroxylase in fungi. *Nucleic Acids Res.* **43**, 10026–10038 (2015).
63. De Marco, V. *et al.* Quaternary structure of the human Cdt1-Geminin complex regulates DNA replication licensing. *Proc. Natl. Acad. Sci. USA* **106**, 19807–19812 (2009).
64. Doyle, J.M., Gao, J., Wang, J., Yang, M. & Potts, P.R. MAGE-RING protein complexes comprise a family of E3 ubiquitin ligases. *Mol. Cell* **39**, 963–974 (2010).
65. Wiedemann, C. *et al.* Structure and regulatory role of the C-terminal winged helix domain of the archaeal minichromosome maintenance complex. *Nucleic Acids Res.* **43**, 2958–2967 (2015).
66. Afonine, P.V. *et al.* Towards automated crystallographic structure refinement with phenix.refine. *Acta Crystallogr. D Biol. Crystallogr.* **68**, 352–367 (2012).
67. Adams, P.D. *et al.* PHENIX: a comprehensive Python-based system for macromolecular structure solution. *Acta Crystallogr. D Biol. Crystallogr.* **66**, 213–221 (2010).
68. Chen, V.B. *et al.* MolProbity: all-atom structure validation for macromolecular crystallography. *Acta Crystallogr. D Biol. Crystallogr.* **66**, 12–21 (2010).
69. Amunts, A. *et al.* Structure of the yeast mitochondrial large ribosomal subunit. *Science* **343**, 1485–1489 (2014).
70. Rappsilber, J., Mann, M. & Ishihama, Y. Protocol for micro-purification, enrichment, pre-fractionation and storage of peptides for proteomics using StageTips. *Nat. Protoc.* **2**, 1896–1906 (2007).
71. Chen, Z.A. *et al.* Architecture of the RNA polymerase II-TFIIF complex revealed by cross-linking and mass spectrometry. *EMBO J.* **29**, 717–726 (2010).
72. Cox, J. & Mann, M. MaxQuant enables high peptide identification rates, individualized p.p.b.-range mass accuracies and proteome-wide protein quantification. *Nat. Biotechnol.* **26**, 1367–1372 (2008).